Wave-equation migration velocity analysis — II: Subsalt imaging examples

Geophysical Prospecting, accepted for publication

Paul Sava and Biondo Biondi

Stanford Exploration Project, Mitchell Bldg., Department of Geophysics,

Stanford University, Stanford, CA 94305-2215

(July 22, 2004)

ABSTRACT

Subsalt imaging is strongly dependent on the quality of the velocity model. However, rugose salt bodies complicate wavefield propagation and lead to subsalt multipathing, illumination gaps and shadow zones which cannot be handled correctly by conventional traveltime-based migration velocity analysis. We overcome these limitations by the wave-equation migration velocity analysis technique introduced in a companion paper (Sava and Biondi, 2004) and demonstrate the methodology on a realistic synthetic dataset simulating a salt dome environment and a Gulf of Mexico dataset. We model subsalt propagation using wavepaths created by one-way wavefield extrapolation. Those wavepaths are much more accurate and robust than broadband rays, since they inherit the frequency dependence and multipathing of the underlying wavefield. We formulate an objective function for optimization in the image space by relating an image perturbation to a perturbation of the velocity model. The image perturbations are defined using linearized prestack residual migration, thus ensuring stability relative to the first-order Born approximation assumptions. Synthetic and real data examples demonstrate that wave-equation MVA is an effective tool for subsalt velocity analysis, even when shadows and illumination gaps are present.

INTRODUCTION

Depth imaging of complex structures depends on the quality of the velocity model. However, conventional Migration Velocity Analysis (MVA) procedures often fail when the wavefield exhibits complex multi-pathing caused by strong lateral velocity variations. Imaging under rugged salt bodies is an important case when ray-based MVA methods are not reliable. Sava and Biondi (2004) present the theory and the methodology of an MVA procedure based on wavefield extrapolation with the potential of overcoming the limitations of ray-based MVA methods. In this paper, we present the application of the proposed procedure to Sigsbee 2A, a realistic and challenging 2-D synthetic data set created by the SMAART JV (Paffenholz et al., 2002), and to a 2-D of a 3-D real dataset from the Gulf of Mexico.

Many factors determine the failure of ray-based MVA in a sub-salt environment. Some of them are successfully addressed by our Wave-Equation MVA (WEMVA) method, whereas others, for example the problems that are caused by essential limitations of the recorded reflection data, are only partially solved by WEMVA.

An important practical difficulty encountered when using rays to estimate velocity below rugose salt bodies is the instability of ray tracing. Rough salt topology creates poorly illuminated areas, or even shadow zones, in the subsalt region. The spatial distribution of these poorly illuminated areas is very sensitive to the velocity function. Therefore, it is often extremely difficult to trace rays connecting a given point in the poorly illuminated areas with a given point at the surface (two-point ray-tracing). Wavefield extrapolation methods are robust with respect to shadow zones and they always provide wavepaths usable for velocity inversion.

A related and more fundamental problem with ray-based MVA, is that rays poorly approximate actual wavepaths when a band-limited seismic wave propagates through a rugose top of the salt.

Figure 1 illustrates this issue by showing three band-limited ($1-26$ Hz) wavepaths, also known in in the literature as fat rays or sensitivity kernels (Woodward, 1992; Pratt, 1999; Dahlen et al., 2000). Each of these three wavepaths is associated with the same point source located at the surface but corresponds to a different sub-salt "event". The top panel in Figure 1 shows a wavepath that could be reasonably approximated using the method introduced by Lomax (1994) to trace fat rays using asymptotic methods. In contrast, the wavepaths shown in both the middle and bottom panels in Figure 1 cannot be well approximated using Lomax' method. The amplitude and shapes of these wavepaths are significantly more complex than a simple fattening of a geometrical ray could ever describe. The bottom panel illustrates the worst-case-scenario situation for ray-based tomography because the variability of the top salt topology is at the same scale as the spatial wavelength of the seismic wave. The fundamental reason why true wavepaths cannot be approximated using fattened geometrical ray is that they are frequency dependent. Figure 2 illustrates this dependency by depicting the wavepath shown in the bottom panel of Figure 1 as a function of the temporal bandwidth: $1-5$ Hz (top), $1-16$ Hz (middle), and $1-64$ Hz (bottom). The width of the wavepath decreases as the frequency bandwidth increases, and the focusing/defocussing of energy varies with the frequency bandwidth.

The limited and uneven "illumination" of both the reflectivity model and the velocity model in the subsalt region is a challenging problem for both WEMVA and conventional ray-based MVA (see Figure 7 for an example of this problem). For the reflectors under salt, the angular bandwidth is drastically reduced in the Angle Domain Common Image Gathers (ADCIGs). This phenomenon is caused by a lack of oblique wavepaths in the subsalt, which deteriorates the "sampling" of the velocity variations in the subsalt. Consequently, the velocity inversion is more poorly constrained in the subsalt sediments than in the sediments on the side of the salt body.

Uneven illumination of subsalt reflectors is even more of a challenge than reduced angular cover-

age. It makes the velocity information present in the ADCIGs less reliable by causing discontinuities in the reflection events and creating artifacts. MVA methods assume that when the migration velocity is correct, events are flat in ADCIGs along the aperture-angle axis. Velocity updates are estimated by minimizing curvature of events in ADCIGs. MVA methods may provide biased estimates where uneven illumination creates events that are bending along the aperture-angle axis, even where the image is created with correct velocity. We address this issue by weighting the image perturbations before inverting them into velocity perturbations. Our weights are function of the "reliability" of the moveout measurements in the ADCIGs.

WAVE-EQUATION MVA ALGORITHM

In this section, we briefly summarize the theory of wave-equation migration velocity analysis (WEMVA). In contrast with the companion paper (Sava and Biondi, 2004), we avoid mathematic detail and concentrate on the principles on which WEMVA is developed. Therefore, this section complements the theory presented in Sava and Biondi (2004), and is designed as a quick introduction to WEMVA for the reader less interested in mathematic detail.

The computation of the velocity updates from the results of migrating the data with the current (background) velocity model comprises three main components that are summarized by the flow-chart in Figure 3. The three components are labeled as A, B and C on the chart. Box A corresponds to the computation of the background wavefield, based on the surface data and background slowness. Boxes B and C correspond respectively to the forward and adjoint WEMVA operator.

The data recorded at the surface (D) are downward continued using wavefield extrapolation to all depth levels using the background slowness (S), to generate a background wavefield (U). The known background slowness (S) can incorporate lateral variations. Extrapolation can be done with kernels

corresponding to such methods as Fourier finite-difference (Ristow and Ruhl, 1994), or generalized screen propagator (Rousseau et al., 2003). From the extrapolated wavefield, we can construct the background image (R) by applying a standard imaging condition, for example a simple summation over frequencies.

The background wavefield (U) is an important component of the WEMVA operator. This wavefield plays a role analogous to the one played in traveltime tomography by the ray-field obtained by ray tracing in the background model. The wavefield is the carrier of information and defines the wavepaths along which we spread the velocity errors measured from the migrated images obtained using the background slowness function. The wavefield is band limited, unlike a ray-field which describes propagation of waves with an infinite frequency band. Therefore, the background wavefield provides a more accurate description of wave propagation through complicated media than a corresponding ray-field (Figures 1 and 2). Typical examples are salt bodies characterized by large velocity contrasts where ray tracing is both unstable and inaccurate.

When evaluating the forward operator (Box B), the background wavefield (U) interacts with a slowness perturbation (dS) and generates a scattered wavefield (dW) at every depth level. In our method, scattering is based on the first-order Born approximation, which assumes perturbations to be small both in size and magnitude. This approximation is appropriate, because scattering occurs independently at every depth level. The contribution to the scattered wavefield, is added at each depth level, and the total scattered wavefield (dU) is extrapolated to depth, using the same numerical propagator as the one used to extrapolate the background wavefield from the surface data. Therefore, the wavefield perturbation at any depth level contains the accumulated effects of scattering and extrapolation from all the levels above it. Finally, we apply an imaging condition to the wavefield perturbation (dU) and obtain an image perturbation (dR) corresponding to the slowness perturbation (dS) and the background wavefield (U).

In migration velocity analysis, we are interested in the inverse process, where we take an image perturbation (dR) and construct a slowness perturbation (dS). We obtain image perturbations via image enhancement operators (residual moveout, residual migration etc.) applied to the background image (R). Since the scattering operator is based on the Born approximation, we need to take special precautions to avoid cycle-skipping of phase function. We overcome the Born approximation limitations by using linearized image perturbations, as described by Sava and Biondi (2004).

To invert the linearized image perturbation into slowness updates by an iterative algorithm, such as conjugate gradient (Golub and Loan, 1983), we need to evaluate the adjoint WEMVA operator (Box C) as well as the forward operator. From the image perturbation (dR), we construct an adjoint wavefield perturbation (dU) by applying the adjoint imaging operator. This wavefield is then upward continued to all levels and an adjoint scattered wavefield (dW') is isolated. Finally, using the background wavefield (U), we generate the adjoint slowness perturbation (dS').

Figures 4 and 5 illustrate the flow-chart in Figure 3 by showing its application to two simple examples. In the first example (Figure 4), we use a monochromatic wavefield, whereas in the second one (Figure 5), we use a wide-band wavefield. For both examples the data are recorded above a planar horizontal reflector.

Figure 4a shows a snapshot (taken at time zero) of the monochromatic background wavefield obtained by downward continuation of an incident plane wave in a constant medium. Figure 4b shows a slowness perturbation, that under the influence of the incident wavefield (a), generates a wavefield perturbation (c). The snapshots at zero time shown in panels (a) and (c) can also be regarded as images. Finally, we back-propagate the image perturbation (c) and obtain the adjoint slowness perturbation (d).

Figure 5 shows the analogous panels shown Figure 4, but for wide-band data. Figure 5a shows

the image obtained by wavefield extrapolation of a wide-band plane wave in the background medium. From the same slowness perturbation (b) as in the preceding example, we obtain an image perturbation (c), from which we generate an adjoint slowness perturbation (d) using the background wavefield used to compute the background image.

SUBSALT WAVE-EQUATION MVA

We demonstrate our WEMVA method using synthetic and real datasets corresponding to subsalt environments.

Synthetic example

First, we illustrate our method with a realistic and challenging synthetic data set created by the SMAART JV (Paffenholz et al., 2002). We have used the same model for our sensitivity kernel analysis in the introduction to this paper (Figures 1 and 2). In this section, we concentrate on the lower part of the model, under the salt body. The top panel in Figure 6 shows the background slowness model, and the bottom panel shows the slowness perturbation of the background model relative to the correct slowness. Thus, we simulate a common subsalt velocity analysis situation where the shape of the salt is known, but the smoothly varying slowness subsalt is not fully known. Throughout this example, we denote horizontal location by x and depth by z.

The original data set was computed with a typical marine off-end recording geometry. Preliminary studies of the data demonstrated that in some areas the complex overburden causes events to be reflected with negative reflection angle (i.e. the source and receiver wavepaths cross before reaching the reflector). To avoid losing these events we applied the reciprocity principle and created a split-spread data set from the original off-end data set. This modification of the data set enabled us

to compute symmetric ADCIGs that are easier to visually analyze than the typical one-sided ADCIGs obtained from marine data. Therefore, we display the symmetric ADCIGs in Figure 9 and Figures 13-15. Doubling the dataset also doubles the computational cost of our process.

Figure 7 shows the migrated image using the correct slowness model. The top panel shows the zero offset of the prestack migrated image, and the bottom panel depicts ADCIGs at equally spaced locations in the image. Each ADCIG corresponds roughly to the location right above it.

This image highlights several characteristics of this model that make it a challenge for migration velocity analysis. Most of them are related to the complicated wavepaths in the subsurface under rough salt bodies. First, the angular coverage under salt ($x > 11$ km) is much smaller than in the sedimentary section uncovered by salt ($x < 11$ km). Second, the subsalt region is marked by many illumination gaps or shadow zones, the most striking being located at $x = 12$ and $x = 19$ km. The main consequence is that velocity analysis in the poorly illuminated areas are much less constrained than in the well illuminated zones, as will become apparent later on in our example.

We begin by migrating the data with the background slowness (Figure 8). As before, the top panel shows the zero offset of the prestack migrated image, and the bottom panel depicts angle-domain common image gathers at equally spaced locations in the image. Since the migration velocity is incorrect, the image is defocused and the angle-gathers show significant moveout. Furthermore, the diffractors at depths $z = 7.5$ km, and the fault at $x = 15$ km are defocused.

As described by Sava and Biondi (2004), we run prestack Stolt residual migration for various values of a velocity ratio parameter ρ between 0.9 and 1.6, which ensures that a fairly wide range of the velocity space is spanned. Although residual migration operates on the entire image globally, for display purposes we extract one gather at $x = 10$ km. Figure 9 shows at the top the ADCIGs for all velocity ratios and at the bottom the semblance panels computed from the ADCIGs. We pick

the maximum semblance at all locations and all depths (Figure 10), together with an estimate of the reliability of every picked value which we use as a weighting function on the data residuals during inversion.

Based on the picked velocity ratio, we compute the linearized differential image perturbation, as described in the preceding sections. Next, we invert for the slowness perturbation depicted in the bottom panel of Figure 11. For comparison, the top panel of Figure 11 shows the correct slowness perturbation relative to the correct slowness. We can clearly see the effects of different angular coverage in the subsurface: at $x < 11$ km, the inverted slowness perturbation is better constrained vertically than it is at $x > 11$ km.

Finally, we update the slowness model and remigrate the data (Figure 12). As before, the top panel shows the zero offset of the prestack migrated image, and the bottom panel depicts angle-domain common image gathers at equally spaced locations in the image. With this updated velocity, the reflectors have been repositioned to their correct location, the diffractors at $z = 7.5$ km are focused and the ADCIGs are flatter than in the background image, indicating that our slowness update has improved the quality of the migrated image.

Figures 13-15 show a more detailed analysis of the results of our inversion displayed as ADCIGs at various locations in the image. In each figure, the panels correspond to migration with the correct slowness (left), the background slowness (center), and the updated slowness (right). Figure 13 corresponds to an ADCIG at $x = 8$ km, in the region which is well illuminated. The angle gathers are clean, with clearly identifiable moveouts that are corrected after inversion. Figure 14 corresponds to an ADCIG at $x = 10$ km, in the region with illumination gaps, clearly visible on the strong reflector at $z = 9$ km at a scattering angle of about 20°. The gaps are preserved in the ADCIG from the image migrated with the background slowness, but the moveouts are still easy to identify and correct. Finally,

Figure 15 corresponds to an ADCIG at $x = 12$ km, in a region which is poorly illuminated. In this case, the ADCIG is much noisier and the moveouts are harder to identify and measure. This region also corresponds to the lowest reliability, as indicated by the low weight of the picks (Figure 10). The gathers in this region contribute less to the inversion and the resulting slowness perturbation is mainly controlled by regularization. Despite the noisier gathers, after slowness update and re-migration we recover an image reasonably similar to the one obtained by migration with the correct slowness.

A simple visual comparison of the middle panels with the right and left panels in Figures 13-15 unequivocally demonstrates that our WEMVA method overcomes the limitations related to the linearization of the wave equation by using the first-order Born approximation. The images obtained using the initial velocity model (middle panels) are vertically shifted by several wavelengths with respect to the images obtained using the true velocity (left panels) and the estimated velocity (right panels). If the Born approximation were a limiting factor for the magnitude and spatial extent of the velocity errors that could be estimated with our WEMVA method, we would have been unable to estimate a velocity perturbation sufficient to improve the ADCIGs from the middle panels to the right panels.

Field data example

Our next example concerns a 2-D line extracted from a 3-D subsalt dataset from the Gulf of Mexico. We follow the same methodology as the one used for the preceding synthetic example. In this case, however, we run several non-linear iterations of WEMVA, each involving wavefield linearization, residual migration and inversion.

Figure 16 (top) shows the image migrated with the background velocity superimposed on the background slowness. This image serves as a reference against which we check the results of our

velocity analysis. Two regions of interest are labeled A and B in the figure. The right edge of the model corresponds to a salt body. The top edge of the image is not at the surface, because we have datumed the surface data to a depth below the well-imaged overhanging salt body.

As for the preceding example, we run residual migration and analyze the moveouts of ADCIGs. Figure 17 shows this analysis at one location in the left part of the model. The left panel shows this ADCIG changing according to the velocity ratio parameter, while the right panel shows the semblance scan corresponding to each of these ratios. The overlain line is a pick of maximum semblance, indicating the flattest ADCIG at every depth level. This analysis is repeated at every location from which we obtain two maps: a map of the residual migration parameter at every location in the image (Figure 16, middle), and a map of the weight indicating the reliability of the picks (Figure 16, bottom). The residual migration parameter is plotted relative to 1 (indicated in white), therefore the whiter the map, the flatter the ADCIGs. Overlain is the stack of the background images for visual identification of image features. Next, we generate an image perturbation based on the residual migration picks in Figure 16 (middle) and invert for slowness perturbation using the weights in Figure 16 (bottom) as an approximation for the inverse data covariance matrix.

The results obtained after two non-linear iterations of WEMVA are shown in Figures 18 and 19. As for Figure 16, the three panels show the migrated image superimposed on slowness (top), residual migration picks (middle), and pick weights (bottom). Two regions in which changes occur are labeled A and B.

For both iterations 1 and 2, the residual migration picks converge toward 1, indicating flatter ADCIGs, therefore better focused images. Reflectors in both regions shift vertically, according to the slowness changes. A notable feature is the improved continuity of the strongest reflectors in the region labeled B.

Both image improve after migration with the updated slownesses from WEMVA. However, there are regions where the image changes are small, if at all present. For example, the region to the left of "B", which corresponds to a shadow zone caused by the salt structure in the upper part of the model, does not change. Better velocity could be estimated in this region with 3-D data, since the shadow zones have three-dimensional expressions.

CONCLUSIONS

Subsalt imaging is one of the most challenging problems of modern seismic imaging because the sharp and irregular salt-sediments interface causes multipathing and uneven illumination. Wavefield-continuation migration methods produce high-quality images under salt, but the estimation of the migration velocity function in the subsalt is an unresolved problem. Conventional MVA methods based on traveltimes computed by ray tracing often fail to provide reliable velocity estimates because ray tracing is unstable and sensitive to the fine details of the salt-sediment interface.

In this paper, we demonstrate that the Wave-Equation Migration Velocity Analysis (WEMVA) method (Sava and Biondi, 2004) overcomes many of the problems encountered by ray-based MVA methods when estimating velocity under salt. We use a complex and realistic subsalt datasets to test our methodology. We also illustrate with numerical examples that wavepaths computed by wavefield extrapolation are robust with respect to shadow zones, and they model the finite-frequency wave propagation that occurs in such environments better than rays do. We demonstrate that velocity errors can be effectively measured by residual migration scans. These scans provide useful velocity information almost in all the subsalt areas, although the reliability of these measurements decreases where poor illumination drastically deteriorates the quality of the Angle Domain Common Image Gathers.

To verify that our proposed methodology is capable of overcoming the limitations of the first-order Born approximation, we test the convergence of WEMVA in presence of large velocity anomalies. The magnitude and spatial extents of the anomalies are such that reflectors in the migrated images shift by several wavelengths. Notwithstanding these large shifts, WEMVA converges to an accurate approximation of the true velocity function. Further tests of our WEMVA method on other real datasets are required; however, we believe that such a robust velocity analysis method is an important step forward toward a solution to the subsalt imaging challenges.

ACKNOWLEDGMENT

We would like to acknowledge the financial support of the sponsors of Stanford Exploration Project. BP and ExxonMobil donated the Gulf of Mexico data used in our final example.

REFERENCES

Dahlen, F. A., Hung, S. H., and Nolet, G., 2000, Frechet kernels for finite frequency traveltimes—I. Theory: Geophys. J. Int., **141**, 157–174.

Golub, G. H., and Loan, C. F. V., 1983, Matrix computations: John Hopkins University Press .

Lomax, A., 1994, The wavelength-smoothing method for approximating broad-band wave propagation through complicated velocity structures: Geoph. J. Int., **117**, 313–334.

Paffenholz, J., McLain, B., Zaske, J., and Keliher, P., 2002, Subsalt multiple attenuation and imaging: Observations from the Sigsbee2B synthetic dataset *in* 72nd Ann. Internat. Mtg. Soc. of Expl. Geophys., 2122–2125.

Pratt, R. G., 1999, Seismic waveform inversion in the frequency domain, Part 1: Theory and verification in a physical scale model: Geophysics, **64**, 888–901.

Ristow, D., and Ruhl, T., 1994, Fourier finite-difference migration: Geophysics, **59**, 1882–1893.

Rousseau, J. H. L., Calandra, H., and de Hoop, M. V., 2003, Three-dimensional dept imaging with generalized screens: A salt body case study: Geophysics, **68**, 1132–1139.

Sava, P., and Biondi, B., 2004, Wave-equation migration velocity analysis—I: Theory: Geophysical Prospecting, submitted for publication.

Woodward, M. J., 1992, Wave-equation tomography: Geophysics, **57**, 15–26.

LIST OF FIGURES

5 Wide-band WEMVA example: background image (a), slowness perturbation (b), image perturbation (c), slowness backprojection (d).

6 Sigsbee 2A synthetic model. The background slowness model (top) and the correct slowness perturbation (bottom).

7 Migration with the correct slowness. Sigsbee 2A synthetic model. The zero offset of the prestack migrated image (top) and angle-domain common image gathers at equally spaced locations in the image (bottom). Each ADCIG corresponds roughly to the location right above it.

8 Migration with the background slowness. Sigsbee 2A synthetic model. The zero offset of the prestack migrated image (top) and angle-domain common image gathers at equally spaced locations in the image (bottom). Each ADCIG corresponds roughly to the location right above it.

9 Residual migration for a CIG at $x = 10$ km. Sigsbee 2A synthetic model. The top panel depicts angle-domain common-image gathers for all values of the velocity ratio, and the bottom panel depicts semblance panels used for picking. All gathers are stretched to eliminate the vertical movement corresponding to different migration velocities. The overlain line indicates the picked values at all depths.

10 Sigsbee 2A synthetic model. The top panel depicts the velocity ratio difference $\Delta\rho = 1 - \rho$ at all locations, and the bottom panel depicts a weight indicating the reliability of the picked values at every location. The picks in the shadow zone around $x = 12$ km are less reliable than the picks in the sedimentary region around $x = 8$ km. All picks inside the salt are disregarded.

11 Sigsbee 2A synthetic model. The correct slowness perturbation (top) and the inverted slowness perturbation (bottom).

12 Migration with the updated slowness. Sigsbee 2A synthetic model. The zero offset of the prestack migrated image (top) and angle-domain common image gathers at equally spaced locations in the image (bottom). Each ADCIG corresponds roughly to the location right above it.

13 Angle-domain common-image gathers at $x = 8$ km. Sigsbee 2A synthetic model. Each panel corresponds to a different migration velocity: migration with the correct velocity (left), migration with the background velocity (center) and migration with the updated velocity (right).

14 Angle-domain common-image gathers at $x = 10$ km. Sigsbee 2A synthetic model. Each panel corresponds to a different migration velocity: migration with the correct velocity (left), migration with the background velocity (center) and migration with the updated velocity (right).

15 Angle-domain common-image gathers at $x = 12$ km. Sigsbee 2A synthetic model. Each panel corresponds to a different migration velocity: migration with the correct velocity (left), migration with the background velocity (center) and migration with the updated velocity (right).

16 Gulf of Mexico data. Migrated image superimposed on slowness (top), residual migration picks (middle), and picking weight (bottom). The migration corresponds to the background slowness.

17 Gulf of Mexico data. Residual migration for a common-image gather about one third from the left edge of the image in Figure 16. Angle-domain CIGs (left) and semblance (right) with the picked velocity ratio.

18 Gulf of Mexico data. Migrated image superimposed on slowness (top), residual migration picks (middle), and picking weight (bottom). The migration corresponds to the updated slowness after iteration 1. Compare with Figure 16.

19 Gulf of Mexico data. Migrated image superimposed on slowness (top), residual migration picks (middle), and picking weight (bottom). The migration corresponds to the updated slowness after iteration 2. Compare with Figure 16.

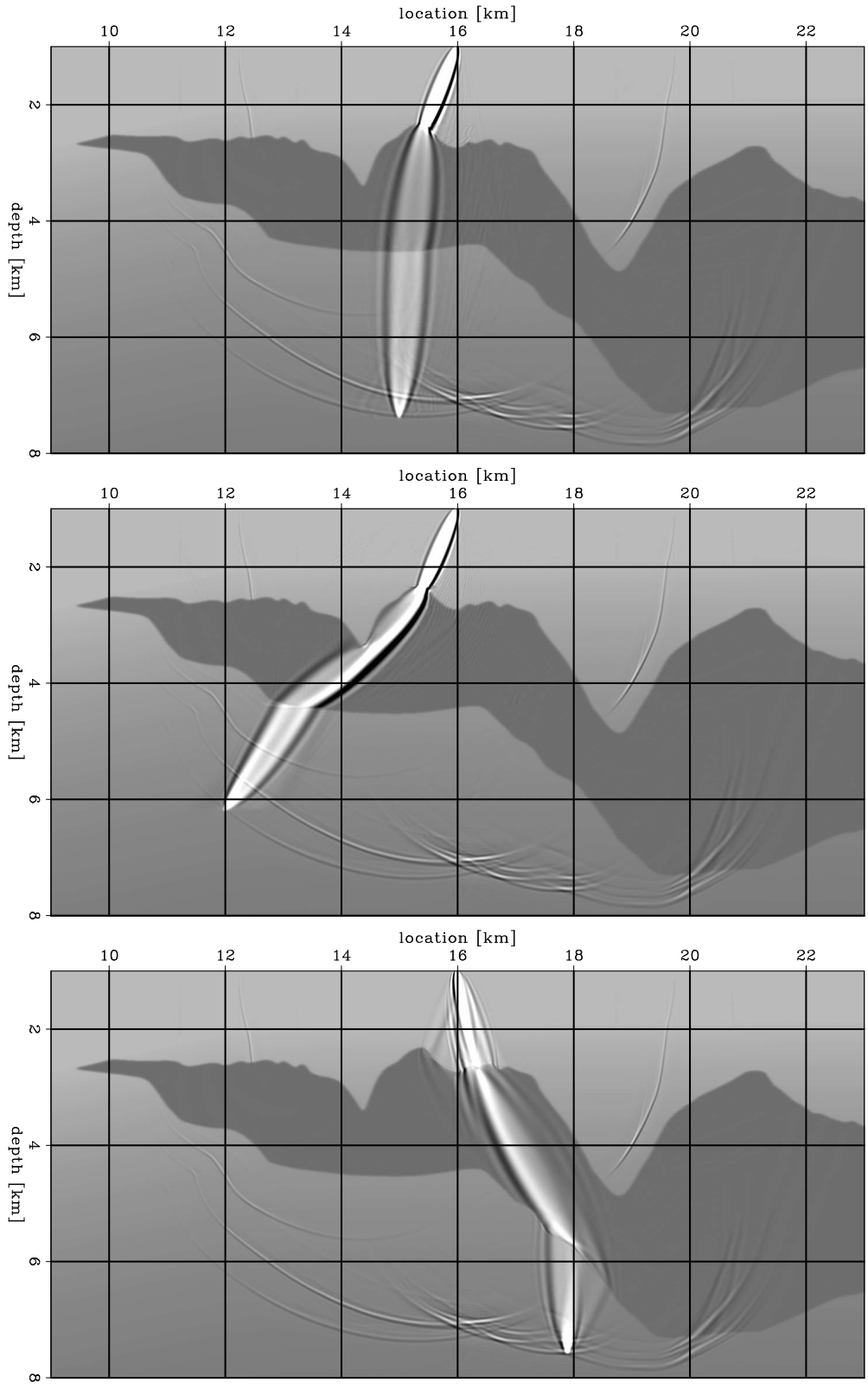
location [km]
10
12
14
16
18
20
22
depth [km]
2
4
6
8
location [km]
10
12
14
16
18
20
22
depth [km]
2
4
6
8
location [km]
10
12
14
16
18
20
22
depth [km]
2
4
6
8

Figure 1.

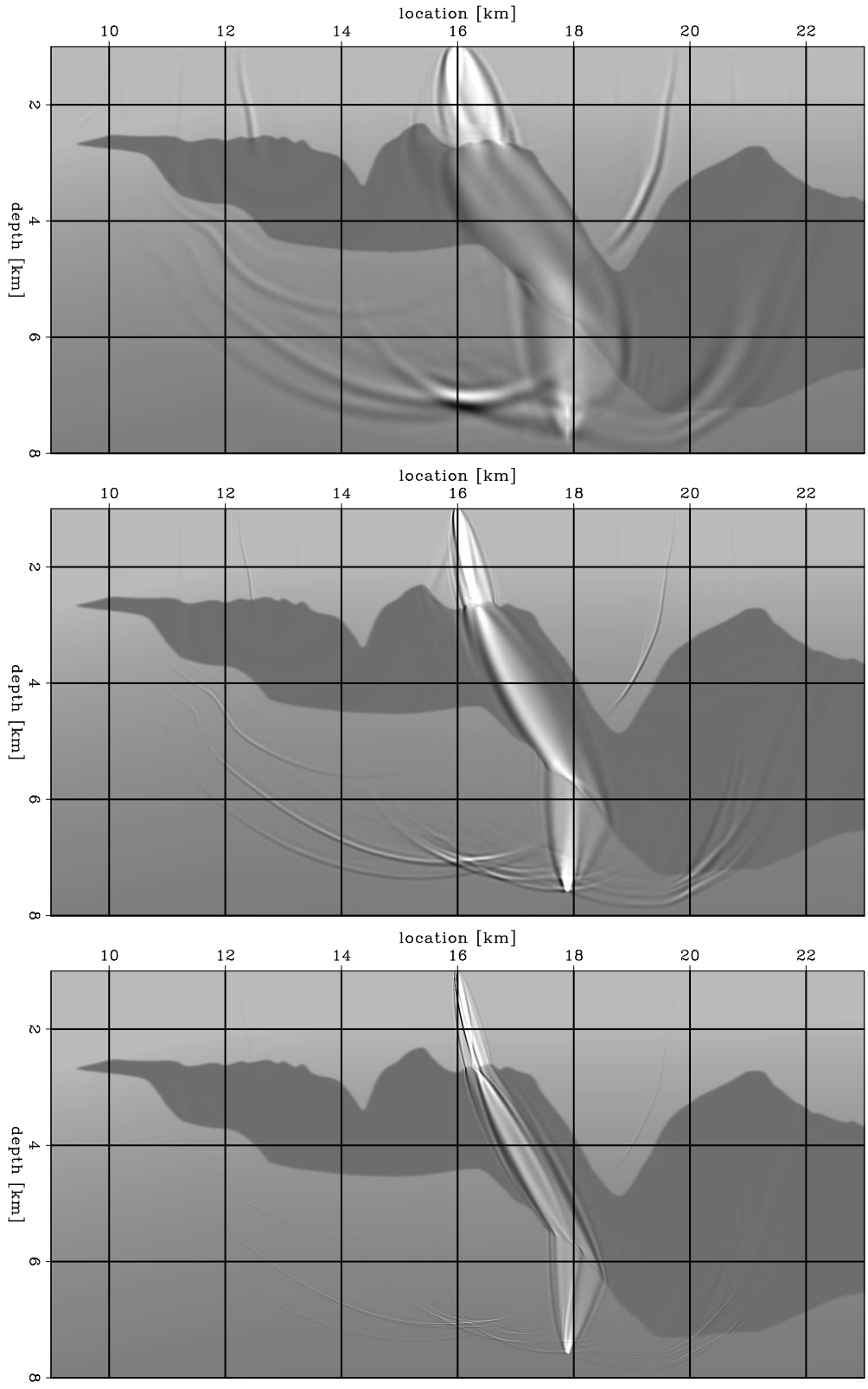
location [km]
10
12
14
16
18
20
22
depth [km]
2
4
6
8
location [km]
10
12
14
16
18
20
22
depth [km]
2
4
6
8
location [km]
10
12
14
16
18
20
22
depth [km]
2
4
6
8

Figure 2.

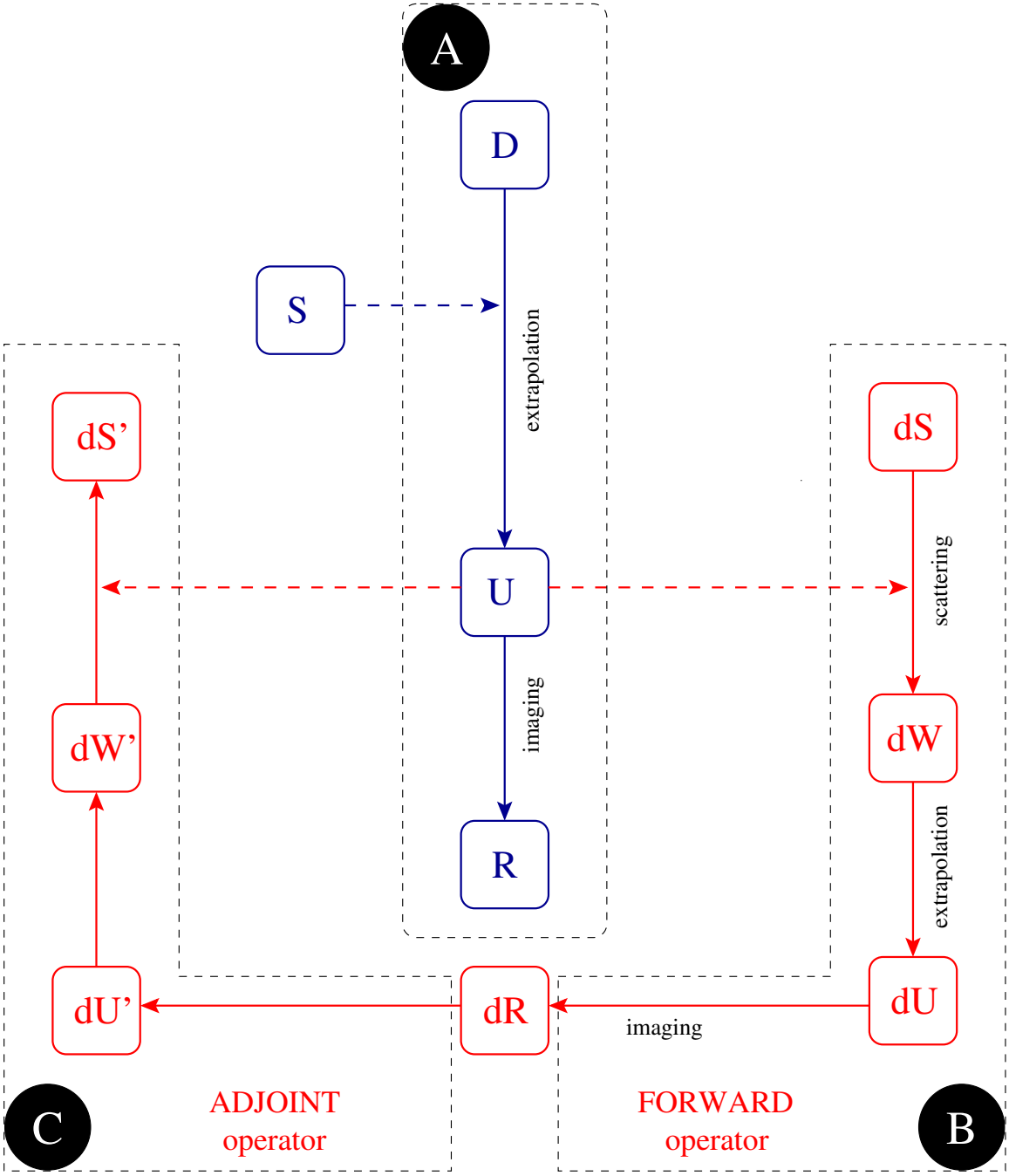
A
D
S
extrapolation
dS'
dS
U
scattering
dW'
dW
imaging
R
extrapolation
dU'
dR
imaging
dU
ADJOINT
operator
FORWARD
operator
C
B

Figure 3.

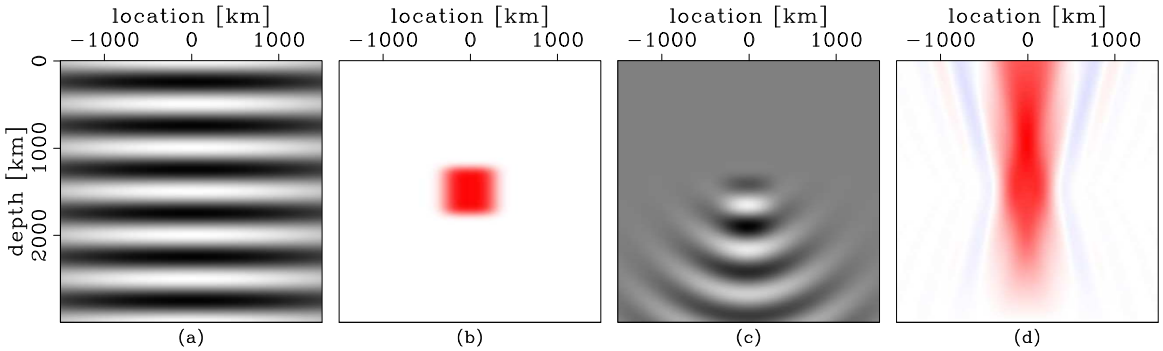

Figure 4.

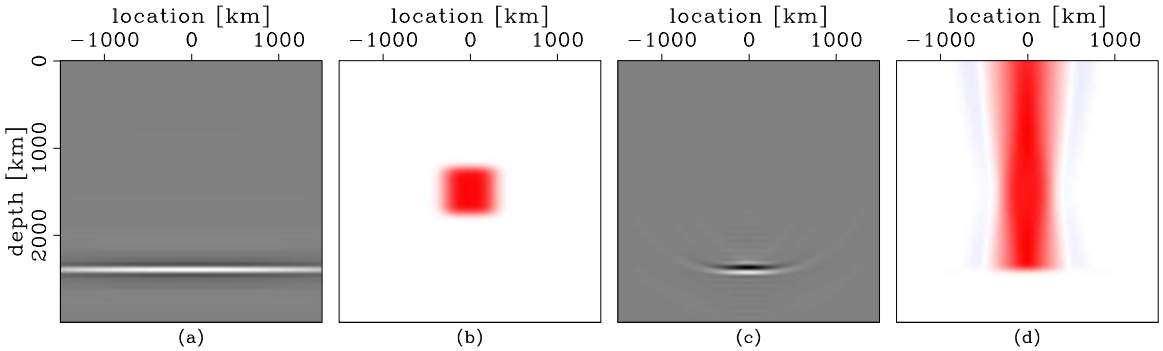

Figure 5.

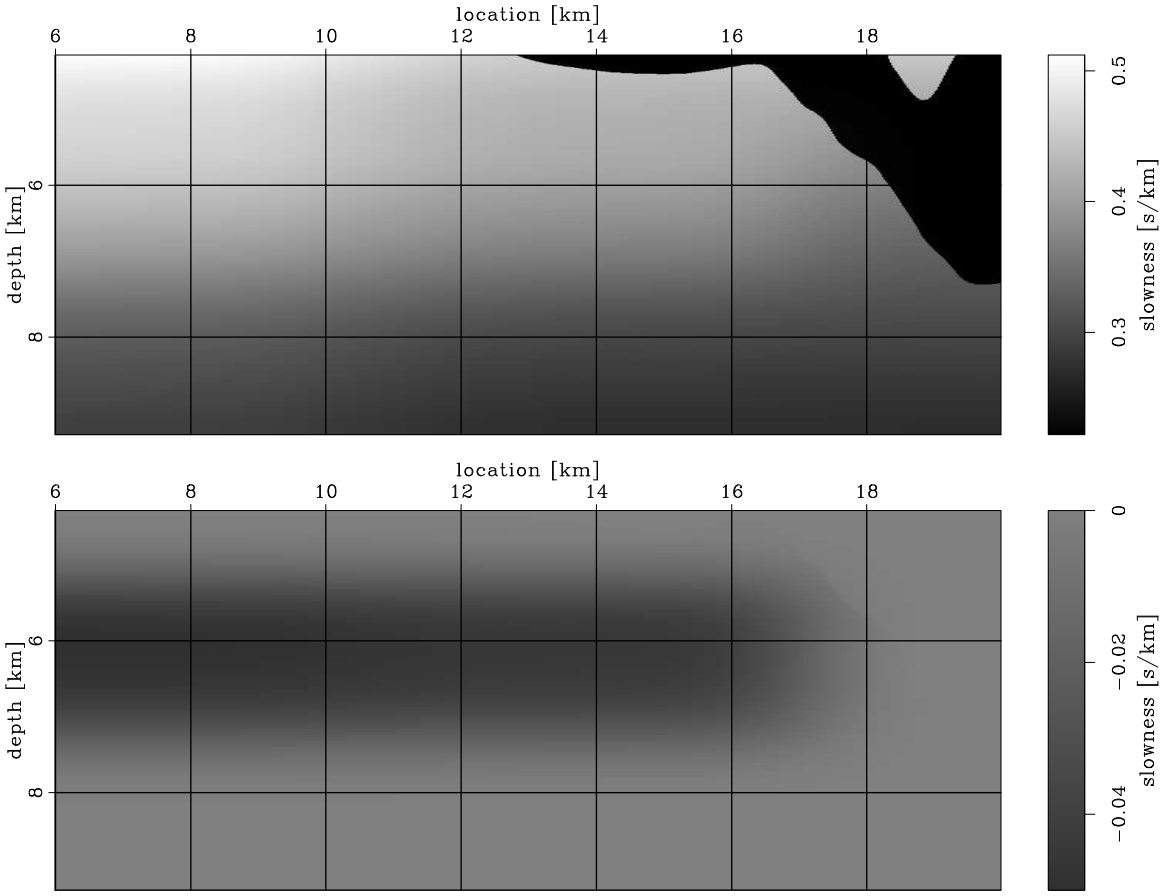
location [km]
6
8
10
12
14
16
18
depth [km]
6
8
0.5
0.4
0.3
slowness [s/km]
location [km]
6
8
10
12
14
16
18
depth [km]
6
8
0
−0.02
−0.04
slowness [s/km]

Figure 6.

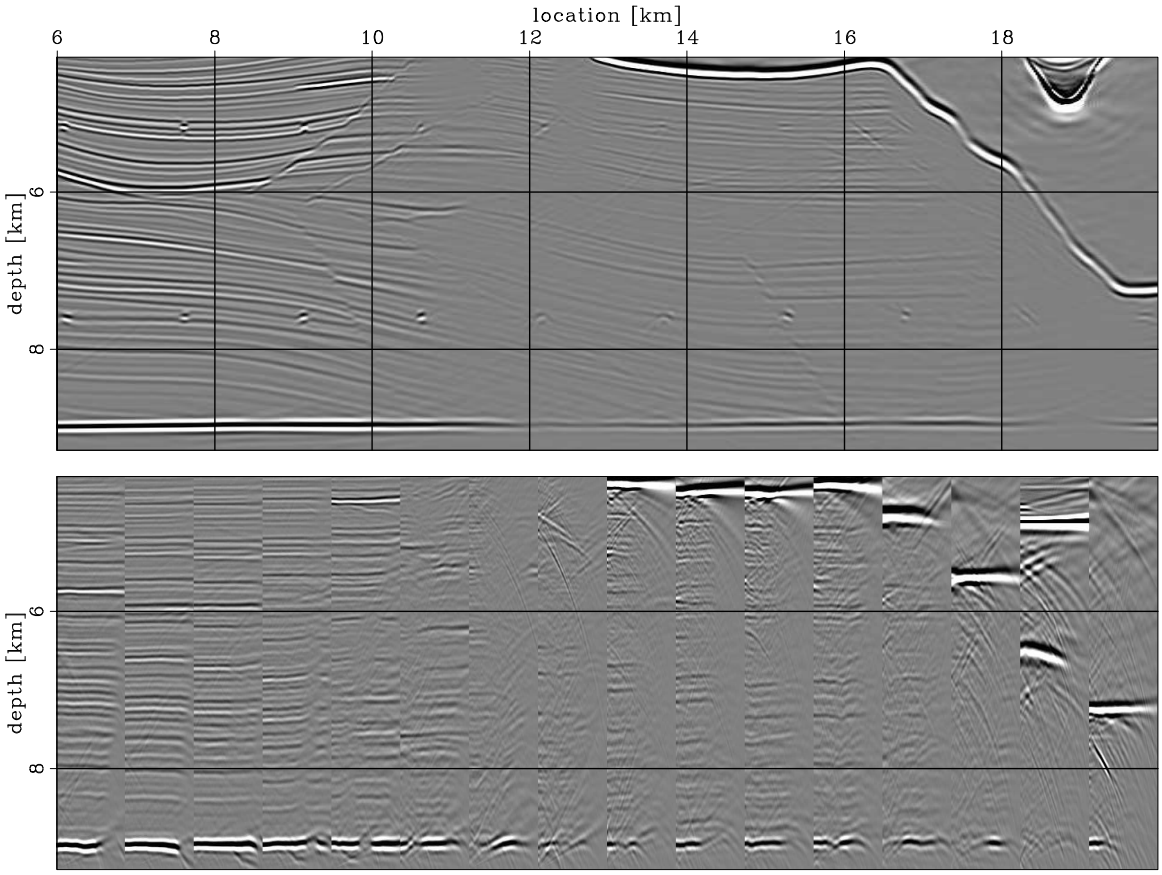

Figure 7.

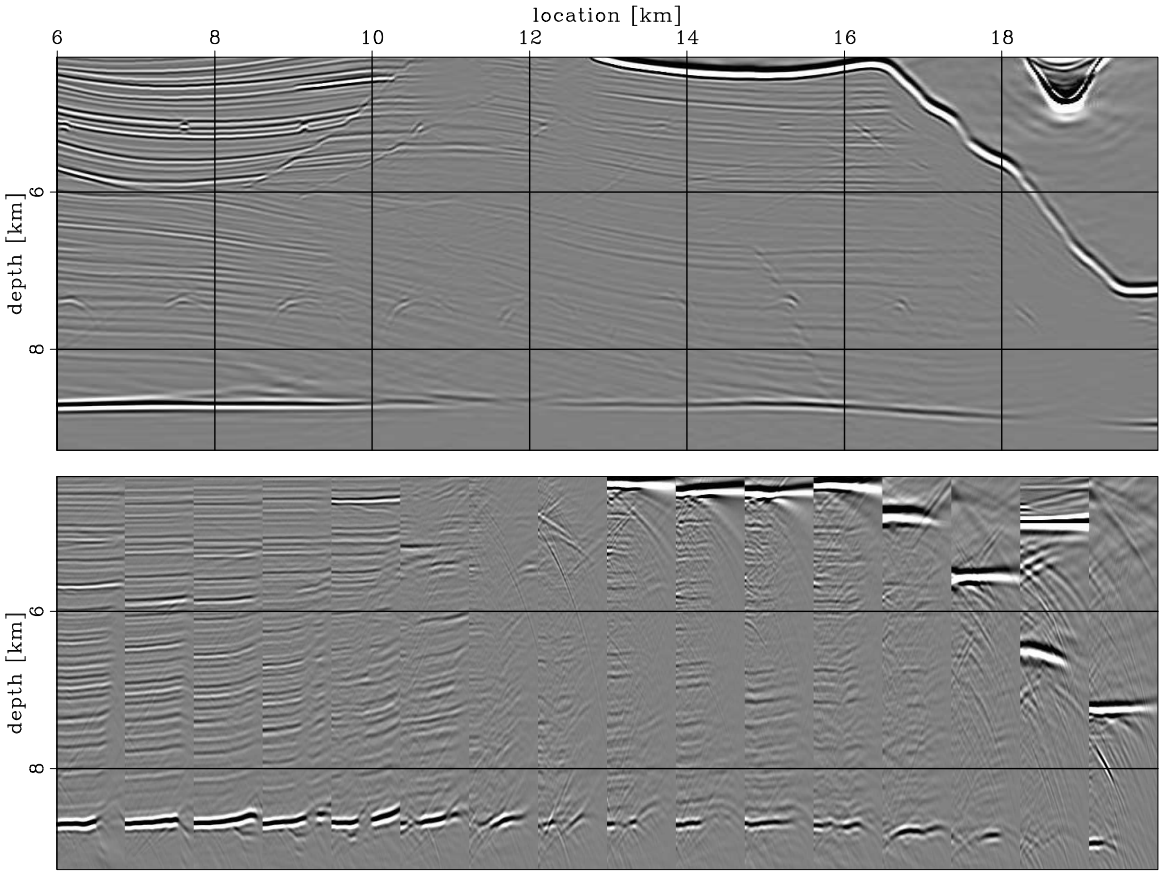

Figure 8.

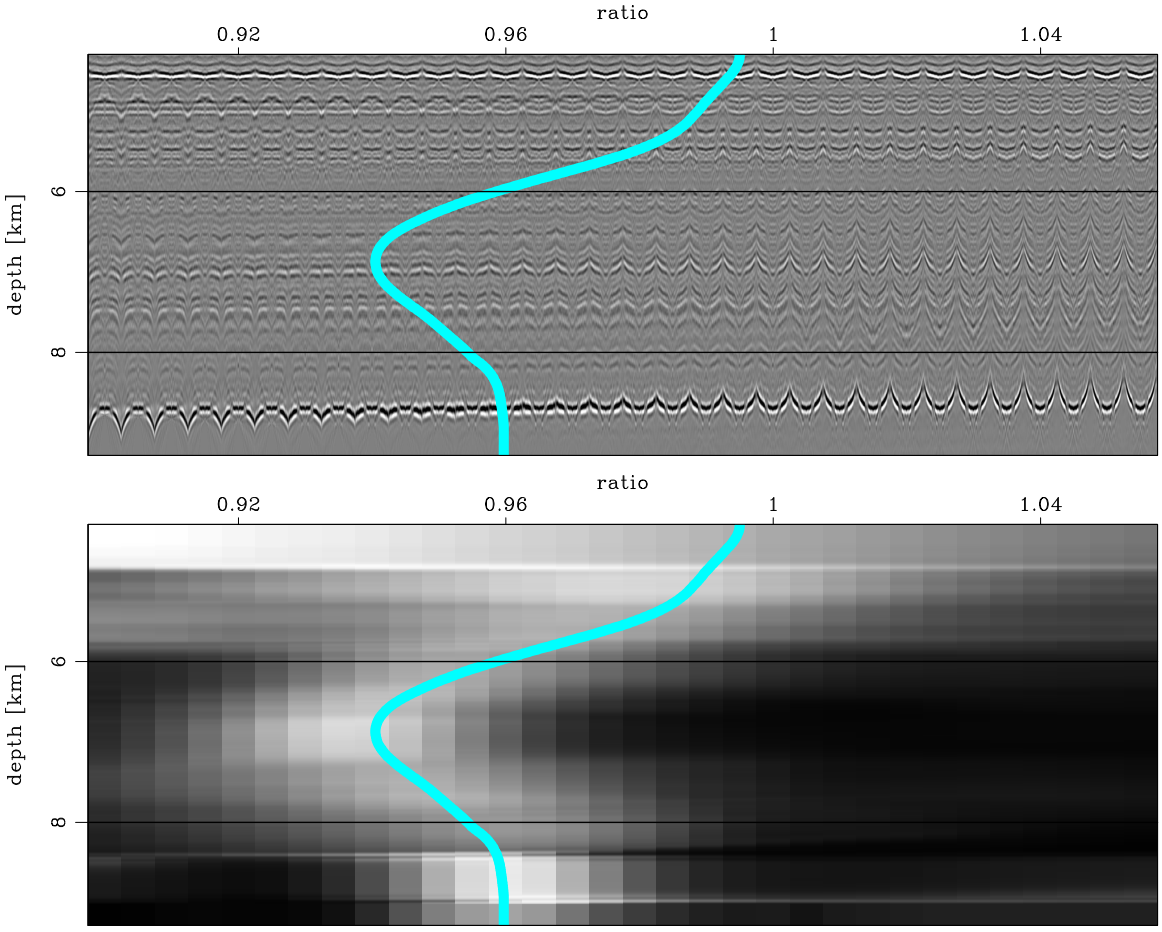

Figure 9.

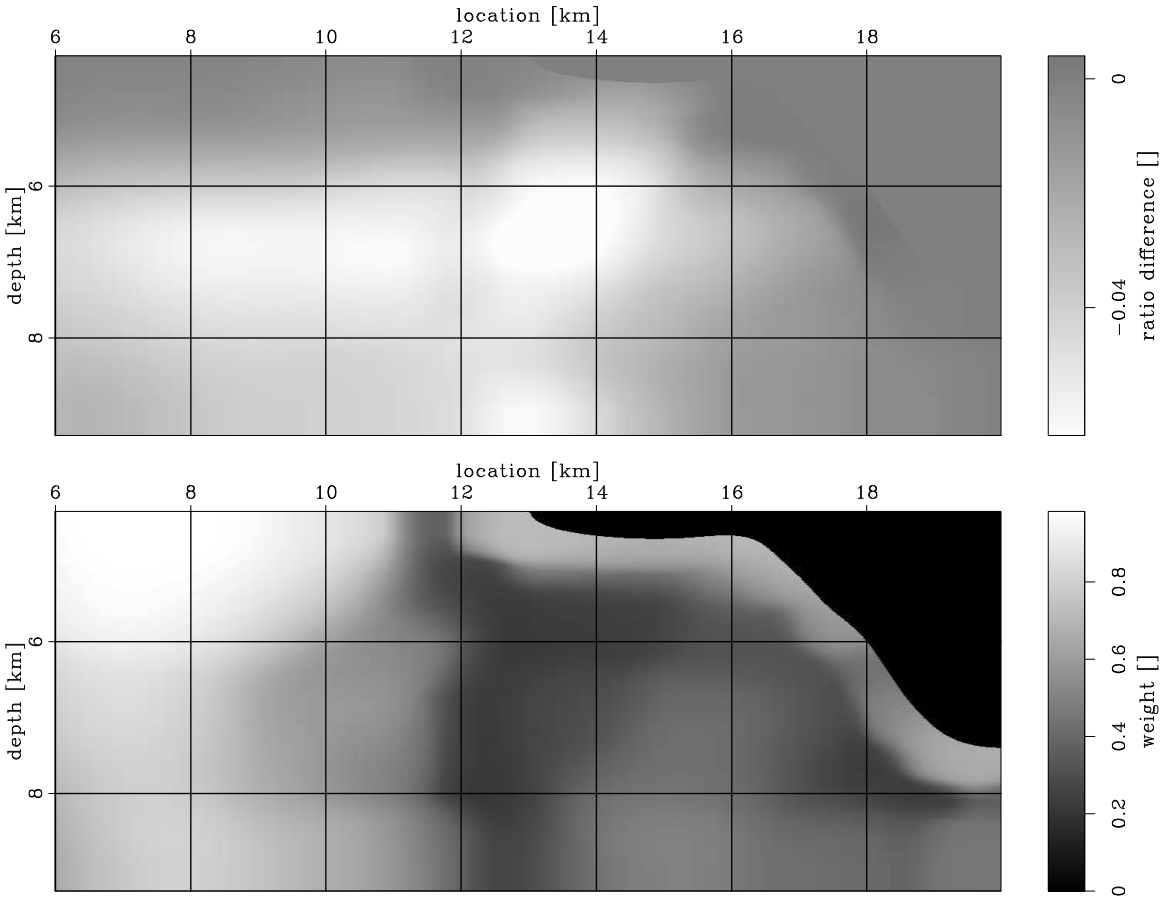
location [km]
6
8
10
12
14
16
18
depth [km]
6
8
ratio difference []
0
−0.04
location [km]
6
8
10
12
14
16
18
depth [km]
6
8
weight []
0
0.2
0.4
0.6
0.8

Figure 10.

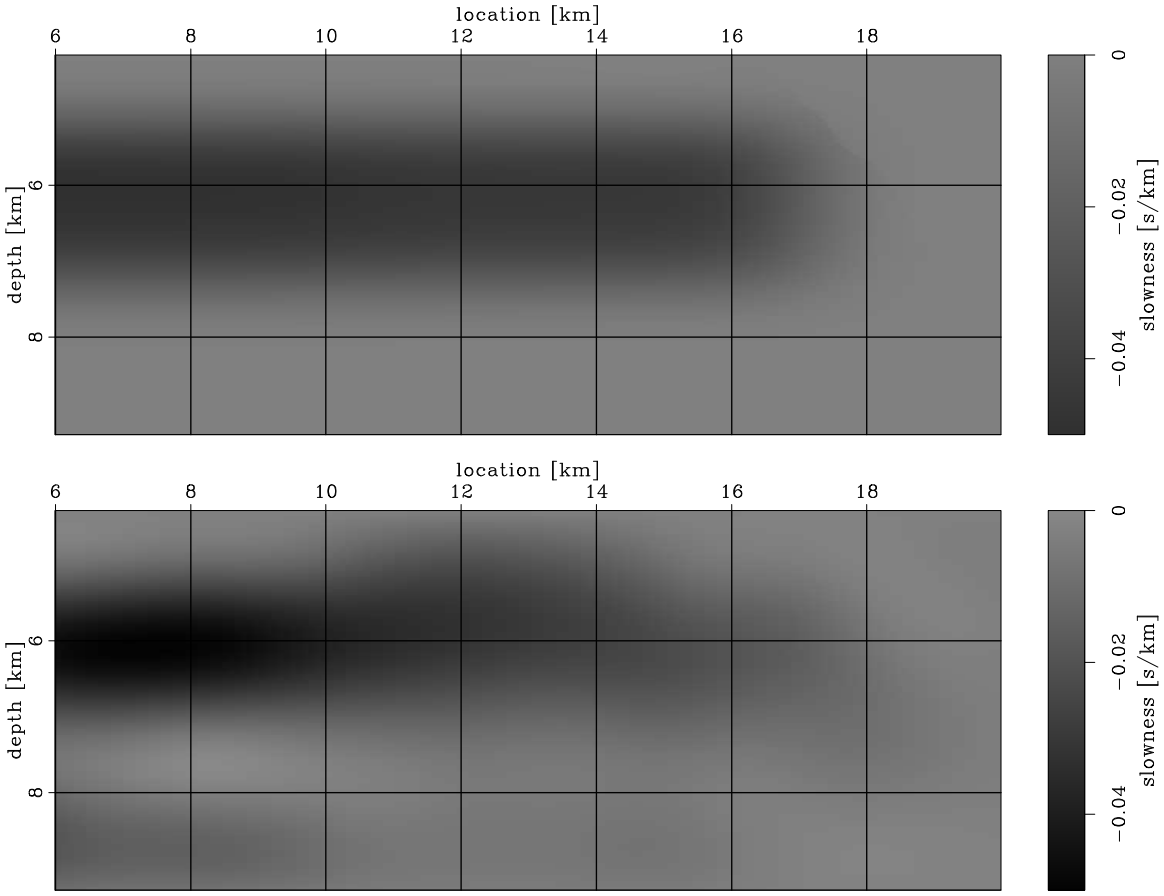
location [km]
6
8
10
12
14
16
18
depth [km]
6
8
slowness [s/km]
0
−0.02
−0.04
location [km]
6
8
10
12
14
16
18
depth [km]
6
8
slowness [s/km]
0
−0.02
−0.04

Figure 11.

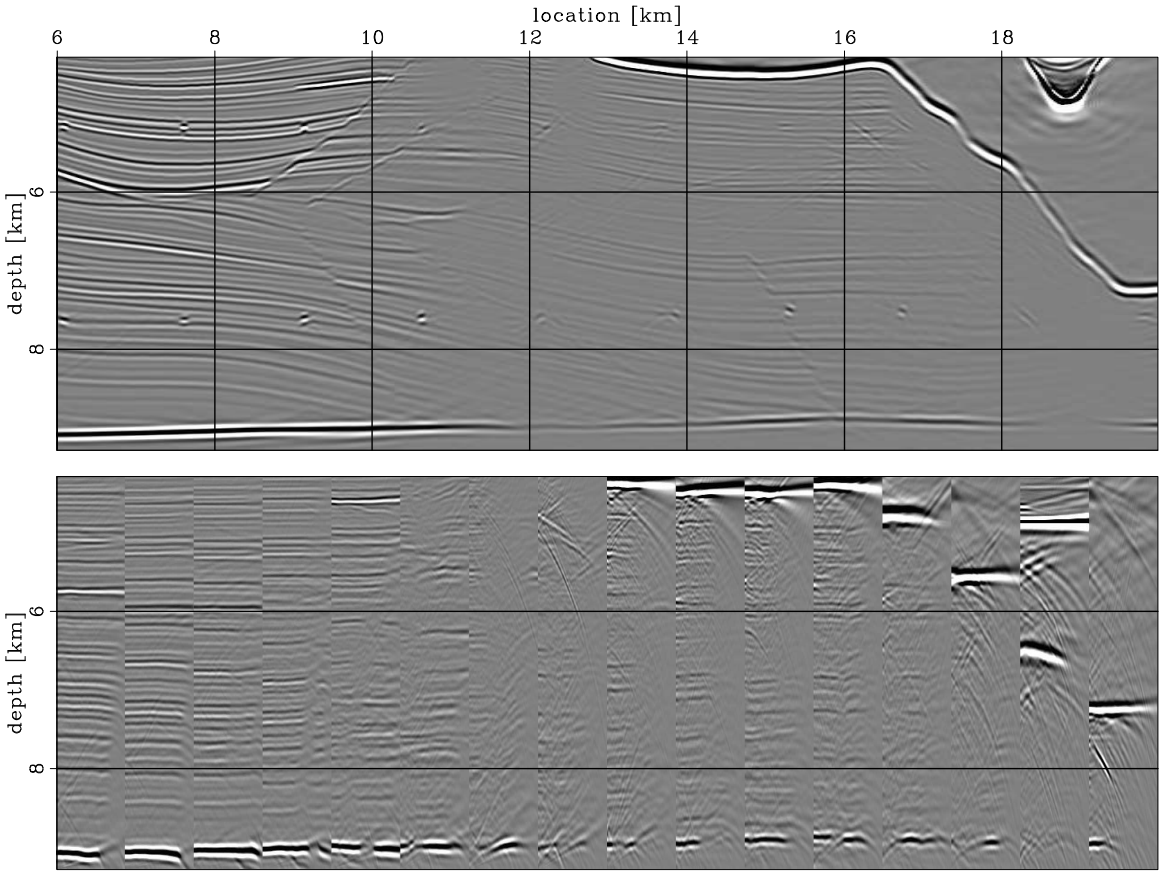

Figure 12.

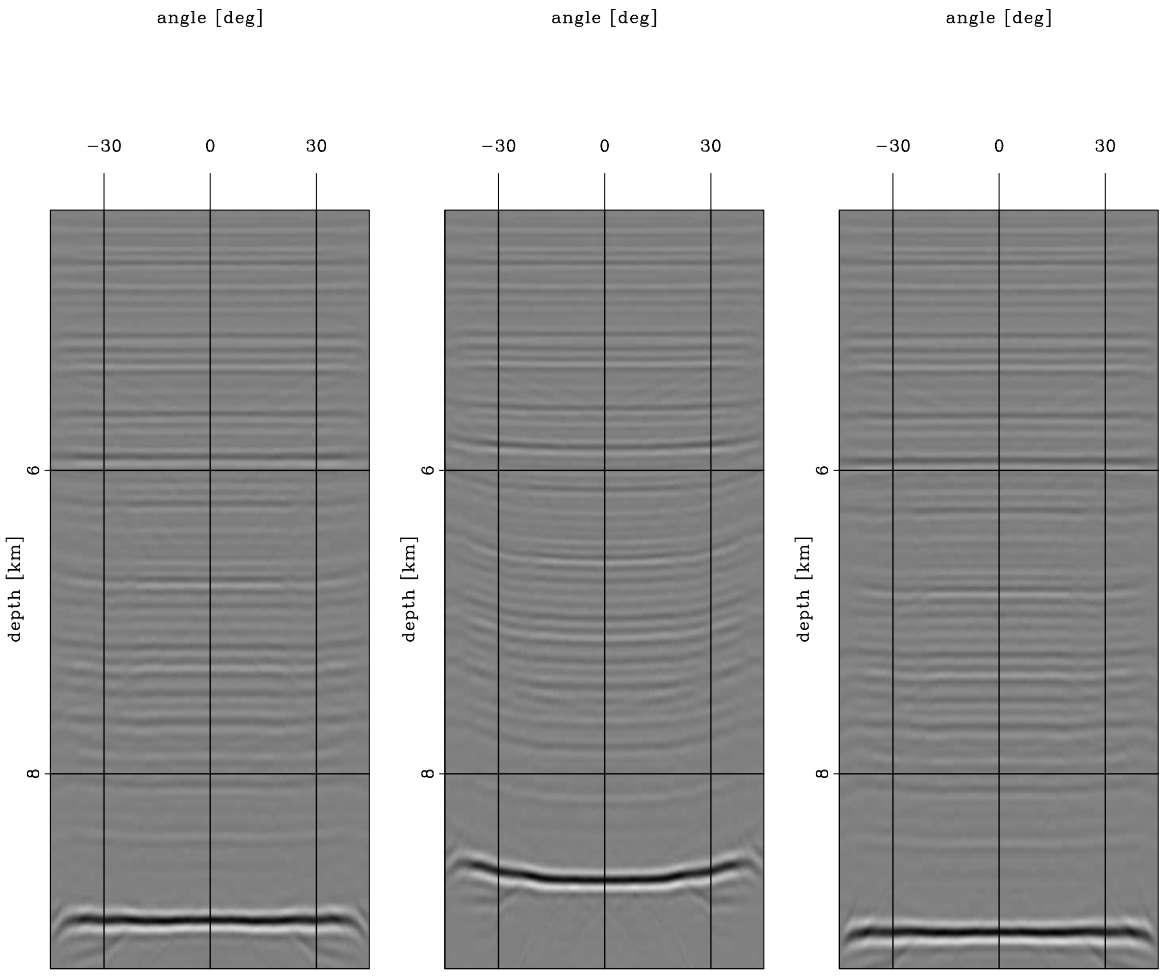

Figure 13.

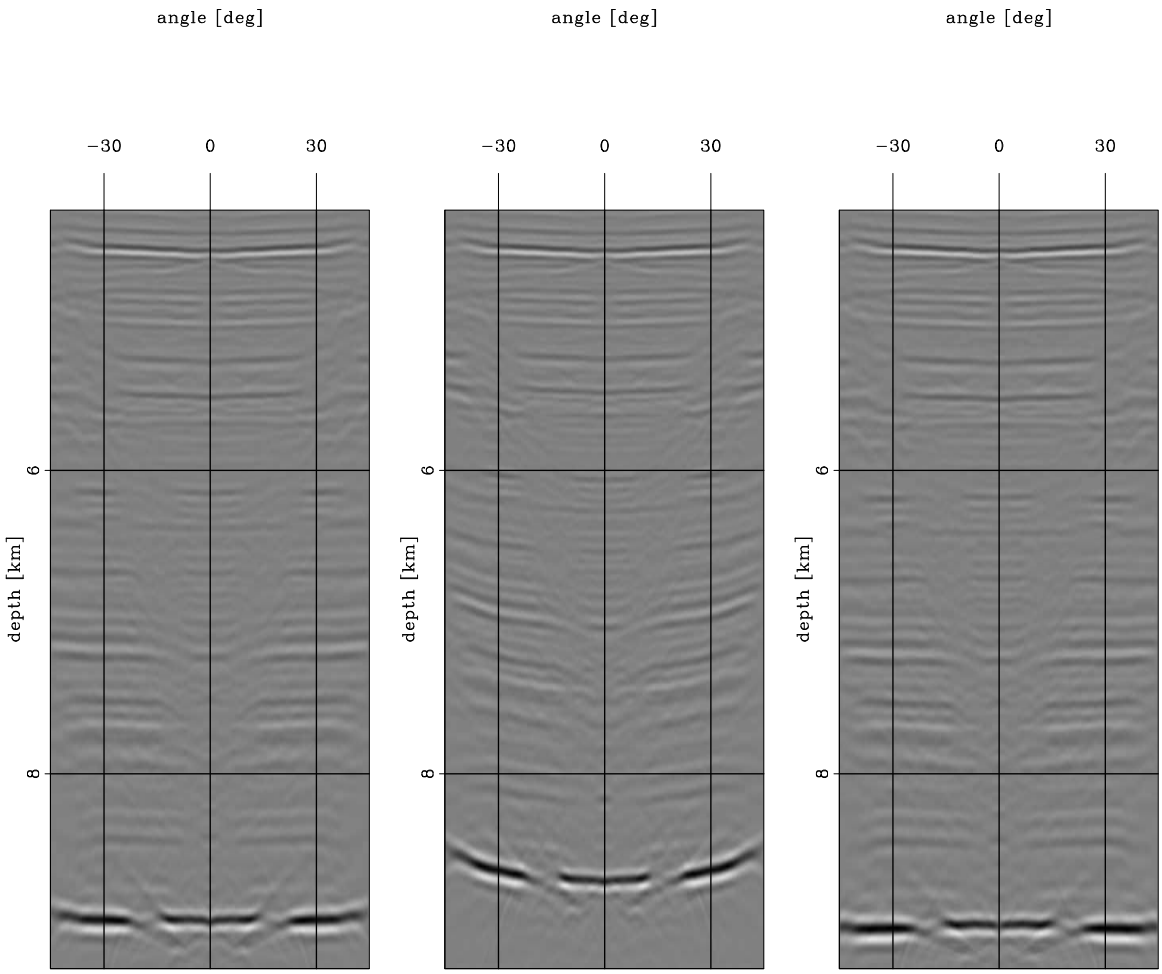

Figure 14.

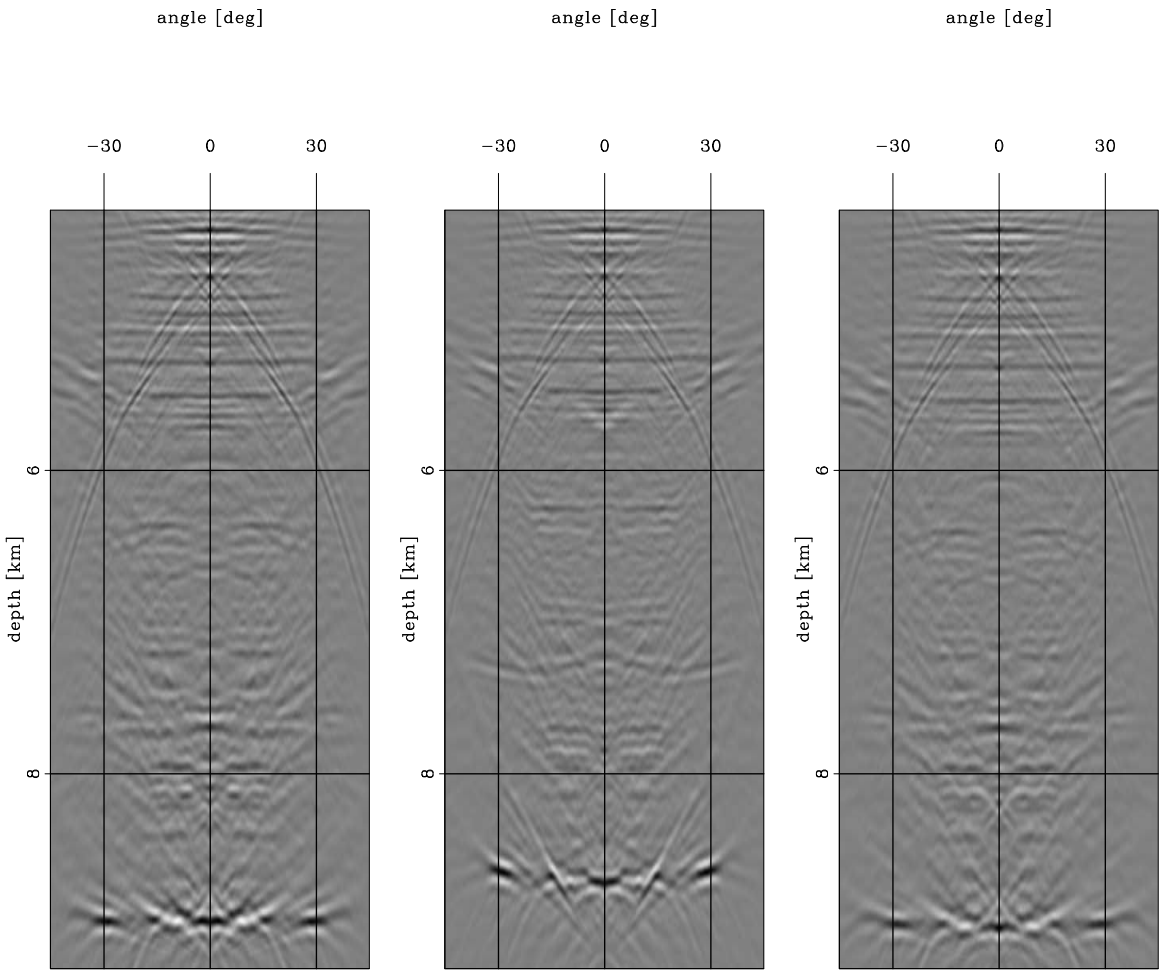

Figure 15.

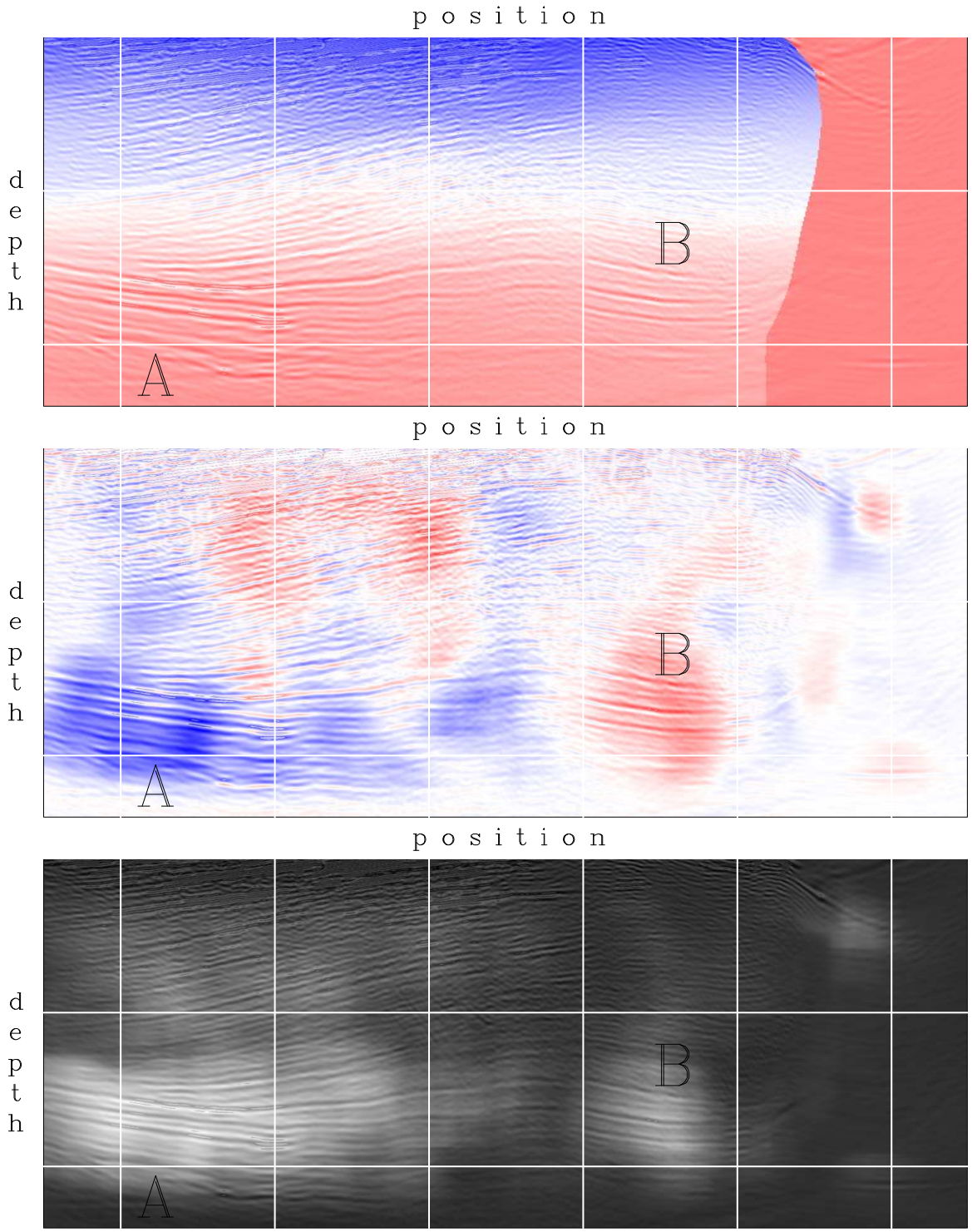

Figure 16.

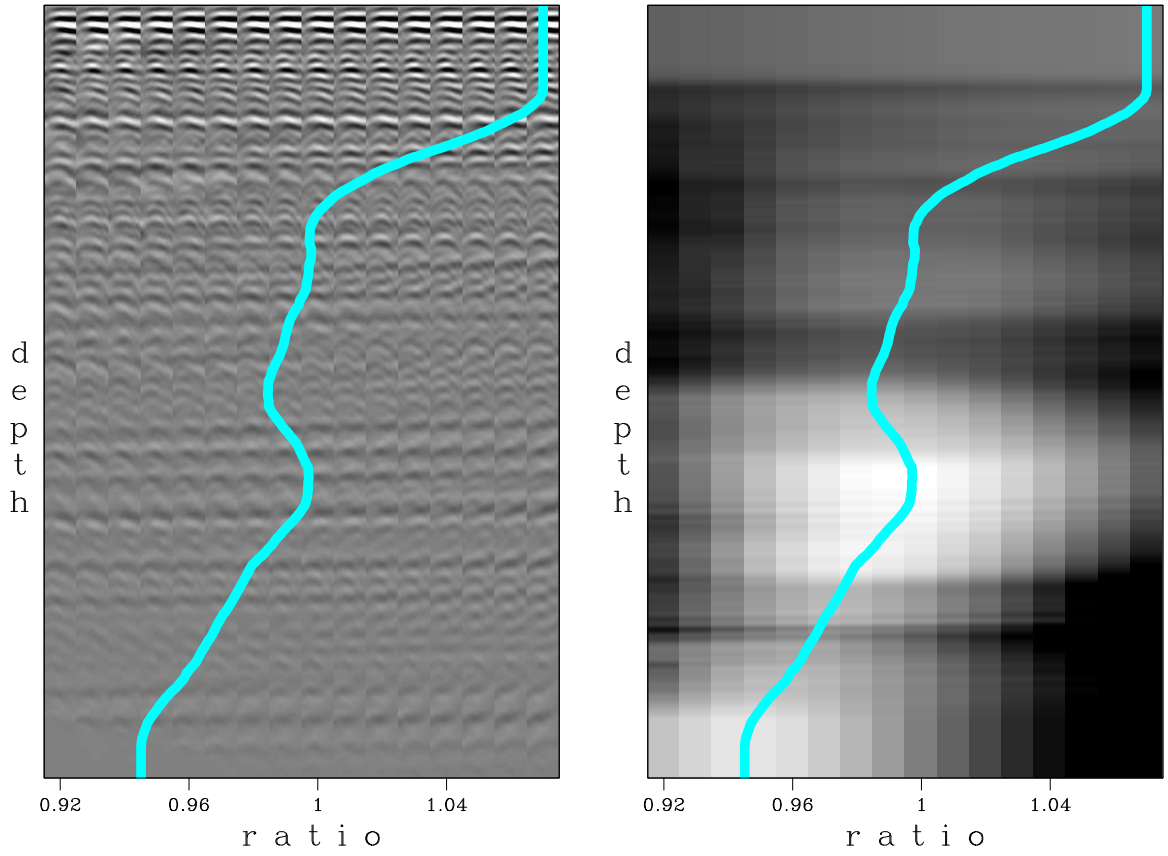

Figure 17.

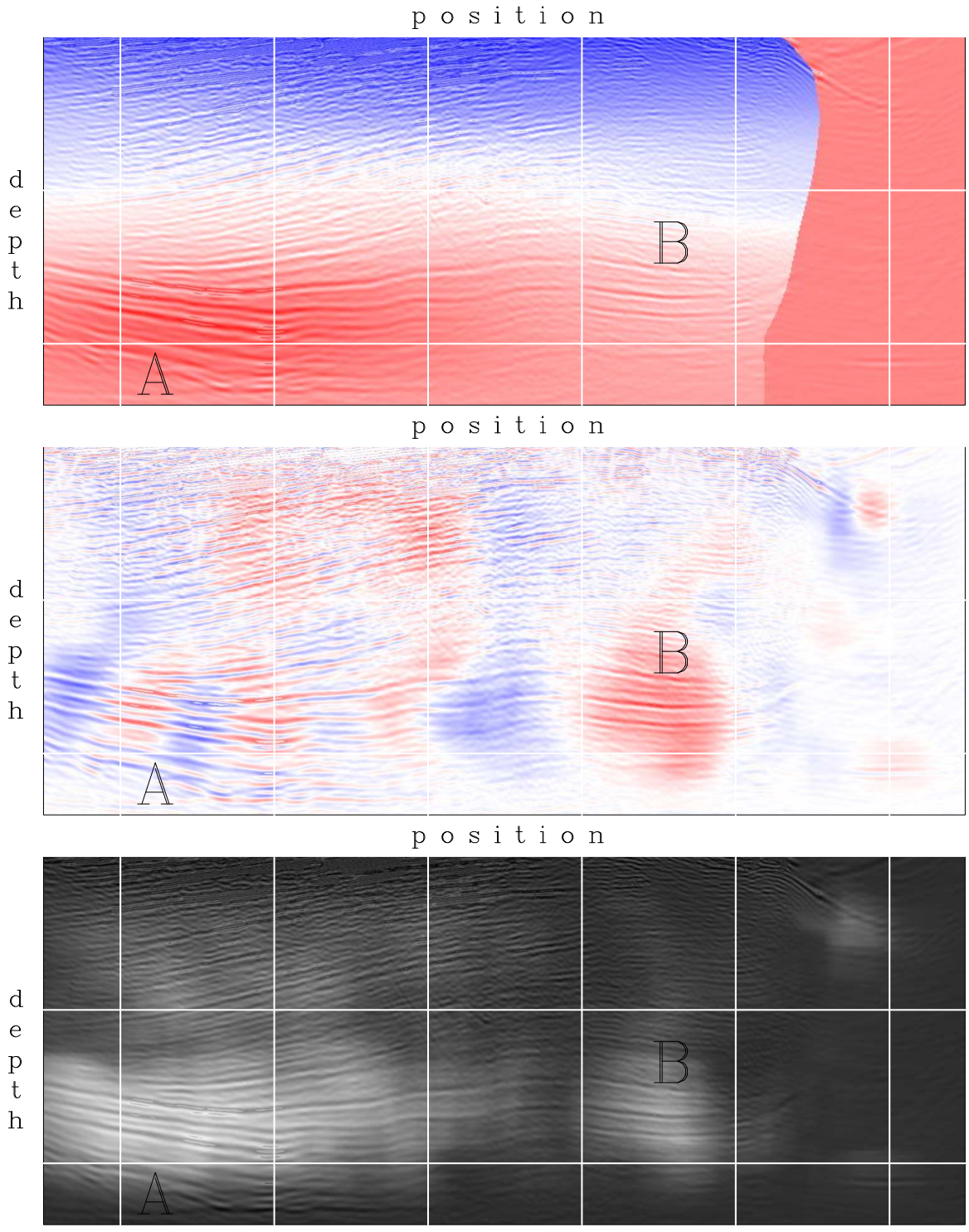

Figure 18.

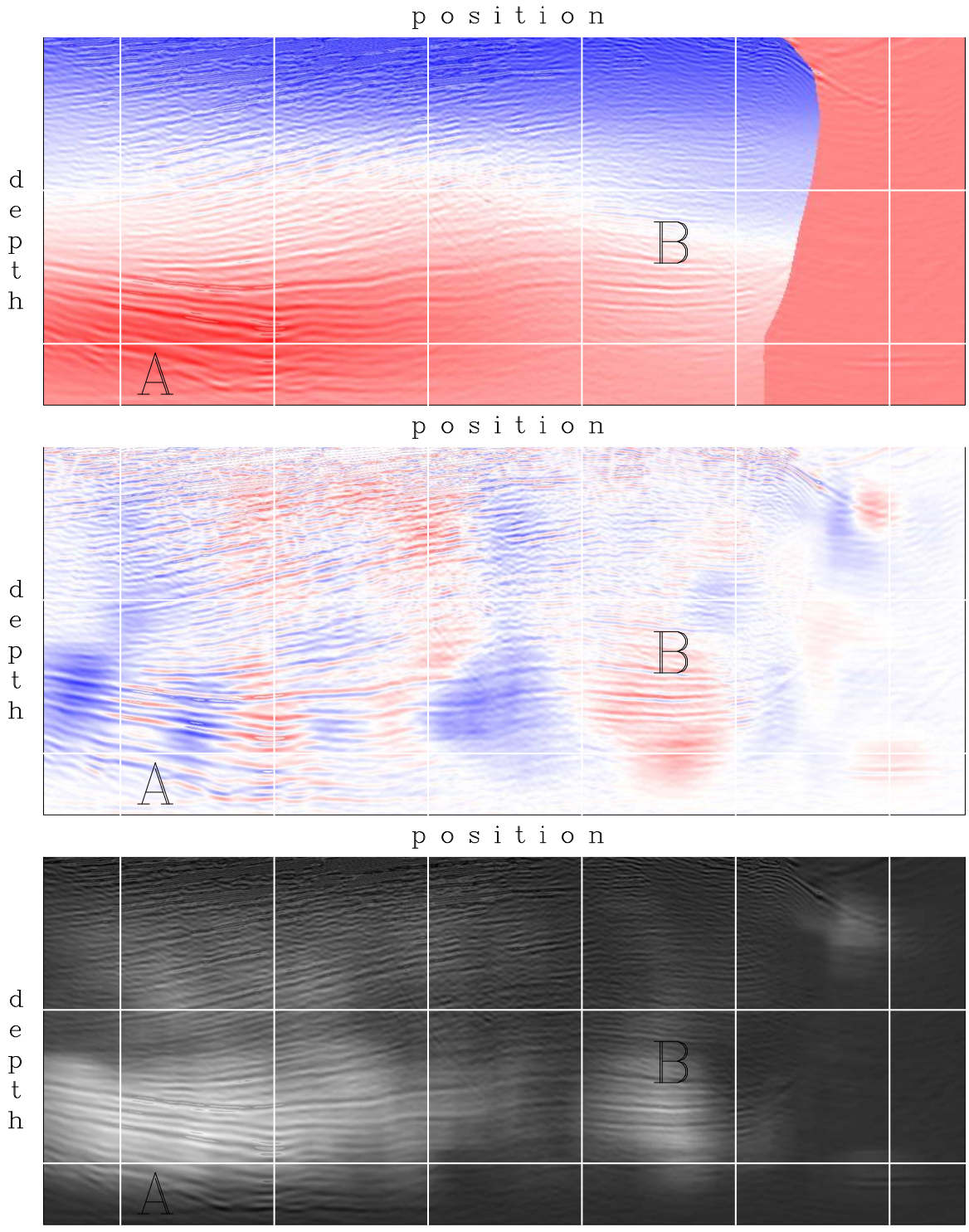

Figure 19.